L-SHAPED CANTILEVER PARALLEL - PLATE MEMS ACCELEROMETER DESIGN PARAMETERS USING A GRAVITATIONAL SEARCH ALGORITHM

Souad Oukil
Electrical Engineering
Faculty USTOMB, BP 1505
El M'Naouar Oran, Algeria.
souad.oukil@yahoo.fr

Abdelmadjid Boudjemai
Centre of Satellite Development (CDS), Space Technology Research Division BP.: 4065 Ibn Rochd USTO Oran, Algeria,
a_boudjemai@yahoo.fr

Nabil Boughanmi
Electrical Engineering
Faculty USTOMB, BP 1505
El M'Naouar Oran, Algeria
boughanminabil@yahoo.com

Submitted: Nov. 12, 2014 ***Accepted: Jan. 7, 2015*** ***Published: Mar. 1, 2015***

Abstract- Due to their small size, low weight, low cost and low energy consumption, MEMS (Micro Electro-Mechanical Systems) accelerometers have achieved great commercial success in recent decades. The objective of this paper is to find the optimum design for a typical MEMS accelerometer, which satisfies a set of given constraints. Due to the complex nature of the problem, a gravitational search algorithm (GSA) is developed for optimization. The GSA attempts to optimize the inter-plate gap while satisfying all other engineering goals. The model was constructed in Msc Patran and Nastran software were calculated and model's response was found. In this paper the optimal design from the theoretically derived gravitational search algorithm is compared to finite element model in order to ascertain its accuracy and verify the results.

Index terms*:* Power system; MEMS; capacitive accelerometer; optimization; proof-mass; L-shaped beam; GSA; frequency.

I. INTRODUCTION

Manufacturing technology microsystems uses micro-technologies for manufacturing integrated circuits including photolithography steps, deposits, and prints. MEMS are currently used to make ink jet printers, accelerometers, inertial sensors, pressure sensors, micro-mirrors, micro-fluidic pumps (figure 1a). New applications such as RF resonators and laboratories on a chip are being developed. MEMS cover various applications in the field of industrial, medical, automotive, telecommunications; defense [1, 2] (figure 1b).

Parallel plate capacitors are widely used in various applications, such as RF devices [3], variable capacitors [4], accelerometers [5, 6, 7], micro-mirrors, and active vibration isolators [8]. One issue that is inherent to all parallel plate actuators (PPA) is the condition of pull-in. Pull-in is the inability of a PPA to be electrostatically actuated beyond one third of its rest gap distance without becoming unstable. Most PPA devices in widespread use are designed so that they only operate while in an open-loop stable range of motion. These devices must be designed so that they are not actuated beyond this point unless additional circuit is added to prevent pull-in from occurring.

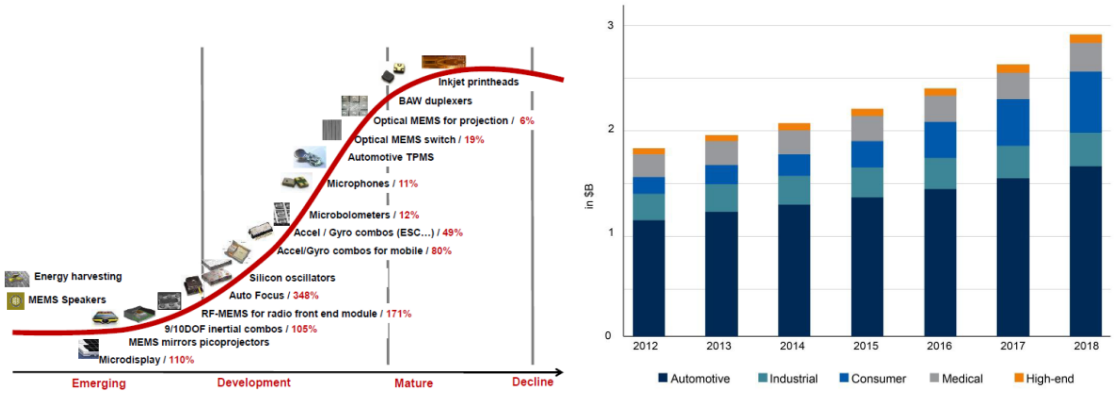

(a) (b)

Figure 1. MEMS evolution: (a) Maturity of MEMS devices [9]; and (b) MEMS sensor by applications [10]

MEMS accelerometers were proposed in 1979 in a paper on a batch-fabricated silicon accelerometer [11]. MEMS based accelerometers are receiving much interest since last few years (see figure 2) [12]. Cost effective and small MEMS accelerometers need for more cost efficient and miniaturized accelerometers are much more demanding in the present scenario. A number of

different accelerometers are available in the market such as capacitive [13], piezoresistive [14] and piezoelectric [15].

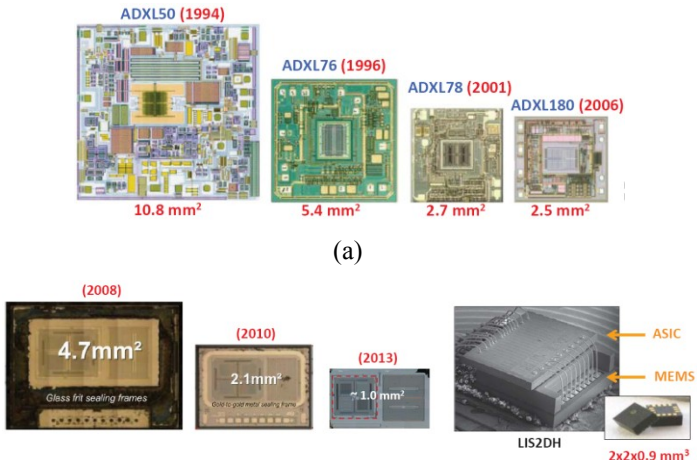

Figure 2. Evolution of MEMS Accelerometers: (a) Analog devises accelerometer (automotive); and (b) STMicroelectronics accelerometer (consumer)

Micromachined accelerometers are extensively used in different areas such as automotive, inertial navigation, guidance, industry, space applications etc (see figure 2). Because of low cost, small size, low power, and high reliability. Among various sensing schemes of accelerometers, capacitive sensing is generally preferred since it provides low temperature dependency, high voltage sensitivity, low noise floor, and low drift. Capacitive accelerometers require special readout electronics to sense the capacitance change and to operate in force-feedback for increased operation range and linearity. With the force-feedback circuit, the overall system becomes complicated because of having both mechanical and electrical components defining the overall performance [16].

In particular the L-shaped cantilever parallel - Plate MEMS are widely used in many area and applications (see figure 3). Many authors have been demonstrating such configuration which gives better sensitivity [17] and suitable for sensing applications. Vincas Benevicius et al. presented in their work an identification of capacitive MEMS accelerometer Structure parameters for human body dynamics measurements, which is used widely in medical applications [18]. D Ozevin et al. consider a device containing an array of MEMS transducers with different resonant

frequencies used for structural health monitoring [19]. MEMS have been proposed for a number of space applications, as lighter and smaller replacement parts or as entire new systems, or as a means to provide affordable redundancy. The L-shaped MEMS sensors are used also in space applications such as sensor placement for structural health monitoring (SHM), damage detection and fault characterization [20, 21, 22, 23, 24, 25].

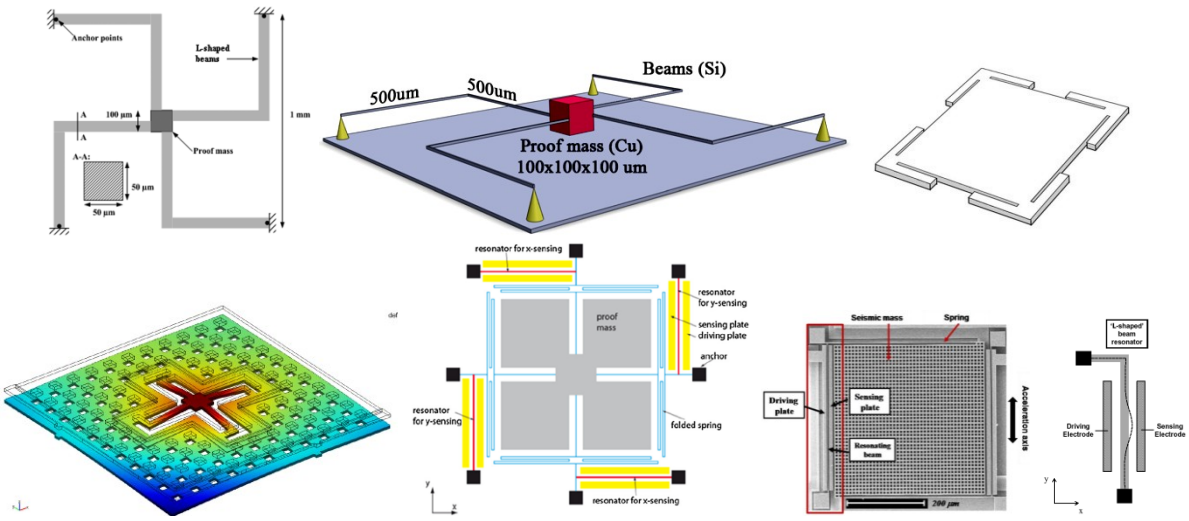

Figure 3. L-shaped cantilever parallel - Plate MEMS accelerometers.

The paper is organized as follows: Parallel - Plate MEMS Accelerometer model are given in Section 2, The gravitational search algorithm is presented in Section 3, Formulation of the objective function of accelerometer model and its validation, are presented in Section 4. Finite element simulations and Modal Analysis of L-shaped cantilever parallel - Plate MEMS accelerometers is given in Section 5. Concluding remarks are provided in the final Section 6.

II. PARALLEL - PLATE MEMS ACCELEROMETER MODEL

II.1 MEMS Accelerometer Mathematical model

The L-shaped cantilever parallel - Plate MEMS accelerometer models used the simulation are shown in Figures 4 and 5, in which the central masses are suspended by flexures that are anchored on substrates. When the structures are exposed to acceleration a , as shown in Figure 4

and 5, whose frequency is much less than the natural frequency of the structure, the masses will be displaced by z for the spring force of the flexures to balance the inertial force. In Figure 5, a plate of mass m and area A is suspended by L - shaped flexures to reduce the nonlinear factor. The plate may be perforated to control the damping factor (or quality factor).

Figure 6 show the design model.

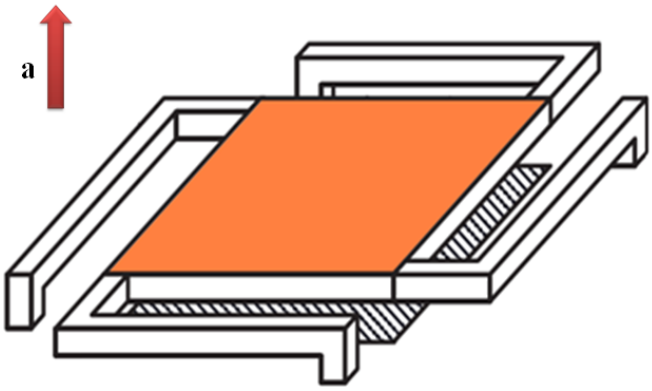

Figure 4. Without Perforated plate.

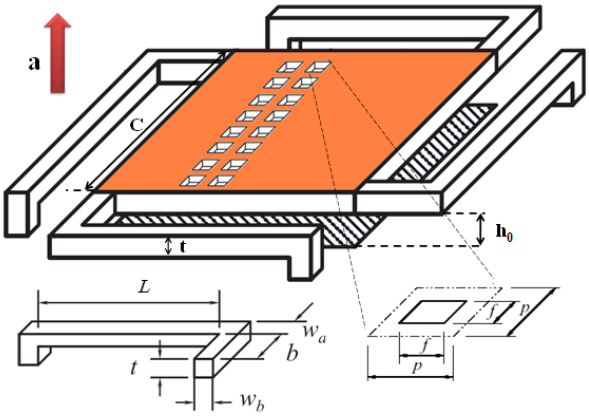

Figure 5. With perforated plate.

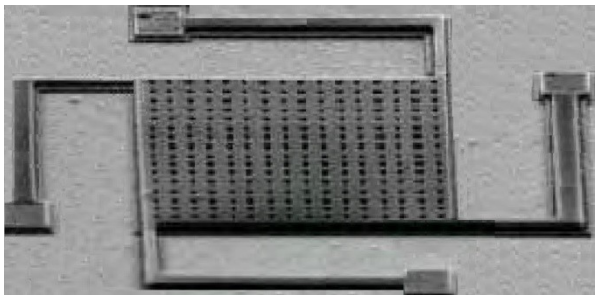

Figure 6. Design model of MEMS Accelerometer

Mathematical model of the designed L-shaped cantilever parallel-plate MEMS accelerometer is similar to vibration equation in [26]. When acceleration is applied to a mass-spring inertial system in the sensing direction, it can be described as follows:

$$mz''+cz'+kz=F_i \tag{1}$$

where m is the proof mass, c presents the damping coefficient, k is the spring constant of the springs, z is the relative displacement of the proof mass and F_i is the applied force which includes electrostatic force and inertia force.

We can set up the model (a parallel - plate actuator) shown in figure 7a to analyze the behavior of the suspended plate. In the model, a suspended plate of mass m and area A is supported by a spring of stiffness k and damper of damping coefficient c , while a voltage less than a pull - in voltage is applied between the suspended and base plates. If the frequency of the applied acceleration a is much less than the natural frequency at V , the spring force balances the inertial force due to the acceleration, and the gap between the plates is changed from the initial gap h_0 to h_a [27].

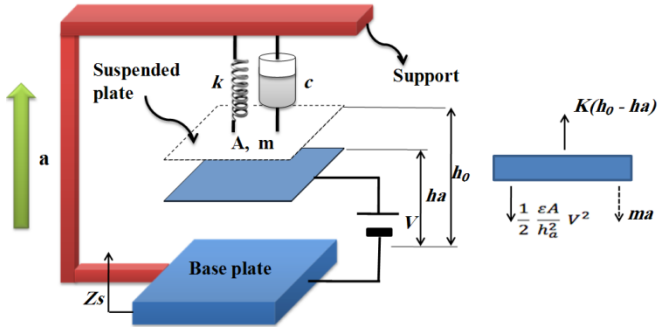

(a) (b)

Figure 7. Model of parallel-plate accelerometer

Referring to the free - body diagram of Figure 7b, we obtain the force equilibrium equation:

$$k(h_0-h_a)=\frac{1}{2}\frac{\varepsilon A}{h_a^2}V^2+ma \tag{2}$$

For convenience, equation (2) may be expressed in a dimensionless form which is given by

$$H_a^3-(1-I)H_a^2+G=0 \tag{3}$$

Where

$$H_a=\frac{h_a}{h_0},\ G=\frac{1}{2}\frac{\varepsilon A}{k h_0^3}V^2,\ I=\frac{ma}{kh_0}$$

The stable solution of the dimensionless force equilibrium equation, (3) is expressed by

$$H_a=\frac{1-I}{3}\left(1+2\cos\left\{\frac{1}{3}\cos^{-1}\left[1-\frac{2}{(1-I)^3}\frac{G}{G_{pi}}\right]\right\}\right) \tag{4}$$

Where G_{pi}= 4/27.

Noted from equation (4) that the two independent parameters I and G affect the dimensionless gap Ha. In Figure 8 the gap Ha is plotted against the inertial force I for the normalized electrostatic force G/G_{pi} = 0, 0.1, 0.2, 0.4, 0.6, 0.8 and 0.95. For G/G_{pi} = 0, the dimensionless gap

H_a decreases linearly from unity to zero because there is no electrostatic force acting on the suspended plate. Physically, this means that the mass moves by maximum displacement (i.e., the initial gap h_0) and touches the base electrode of Figure 7a as the maximum acceleration of kh0/m, corresponding to I = 1, is applied. For $G/G_{pi} \neq 0$, the nonlinear electrostatic force is exerted on the suspended plate and then the parallel - plate actuator can experience pull - in. When the normalized electrostatic force G/G_{pi} increases from zero to unity, the starting gap is lowered from unity and the pull - in gap varies from zero (i.e., the suspended plate touches the base plate) to 2/3.

As the inertial or electrostatic force increases from zero to its pull - in value, the argument of the inverse cosine in (4) varies from unity to negative unity. Therefore, the suspended plate, exposed to the acceleration a, is in a stable or critical condition if the following condition is satisfied:

$$1-\frac{2}{(1-I)^3}\ \frac{G}{G_{pi}} \geq -1 \tag{5}$$

Since equation (5) includes two independent parameters, I and G, the triangle in Figure 8 defines a stable region in which the suspended plate is stable. It is noted that the lower straight line in the figure can be defined as the pull - in gap, at which the suspended plate experiences pull - in. The pull – in gap H_{pi}, inertial force I_{pi} , and electrostatic force G_{pi} play important roles because they provide a guideline for understanding the nonlinear behavior of a parallel - plate actuator under electrostatic force due to a voltage.

The pull - in voltage $V_{pi,a}$ can be extended beyond the pull - in voltage given by

$$V_{pi}=\sqrt{\frac{8kh_0^3}{27\varepsilon A}} \tag{6}$$

which corresponds to the pull - in force G_{pi} at zero acceleration. Thus:

$$V_{pi,a}=\sqrt{2G_{pi}\ \frac{kh_0^3}{\varepsilon A}\ (1-I)^3} = V_{pi}(1-I)^{3/2} \tag{7}$$

Furthermore, it is noted from Figure 9 that the negative dimensionless inertial force increases the gap H_a. In other words, if the L shaped cantilever parallel - plate accelerometer is exposed to a negative acceleration, the voltage and displacement ranges can be extended.

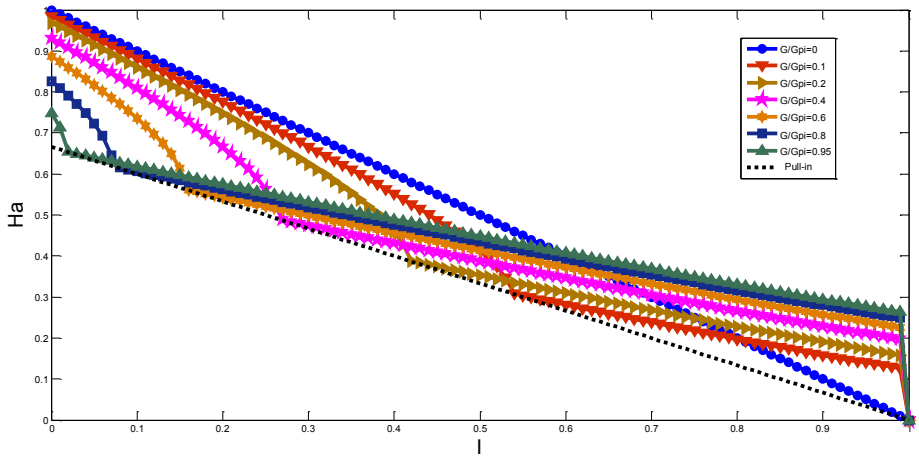

Figure 8. Dimensionless gap H_a with respect to the dimensionless inertial force I and the force G/G_{pi}.

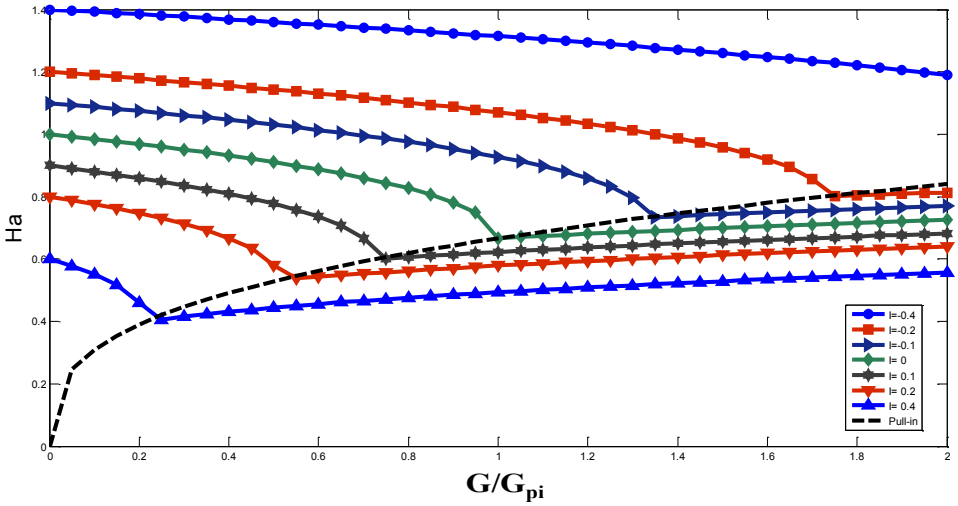

Figure 9. Dimensionless gap H_a with respect to the normalized electrostatic force G/G_{pi} and the dimensionless inertial force I.

The figure 10 shows the three-dimensional variation of dimensionless gap H_a regarding to the G/G_{pi} and I parameters.

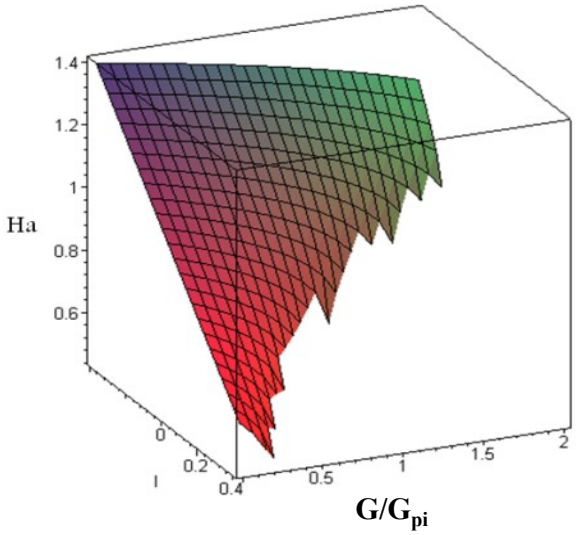

Figure 10. Dimensionless gap H_a with respect to G/G_{pi} and the dimensionless inertial force I.

II.2 Accelerometer model properties

Single crystal silicon material is selected for accelerometer structure. Electrically conductive silicon with resistivity 0.1 Ω-cm is selected for the proof-mass. Similarly Pyrex glass is chosen for top and bottom wafers to reduce stray capacitance and to provide required sealing. The glass wafers are bonded to silicon wafer using anodic bonding process. Electrodes and electrical contact pads are realized by depositing sub-micron thickness Aluminum coating, using E-beam evaporation process. The material properties of silicon and Pyrex glass are shown in table 1.

Table 1: The materials properties.

Material Property	**Silicon**	**Pyrex glass**
σy (yield strength) 10^9 N/m^2	7	0.5-0.7
E (Young's modulus) 10^{11}N/m^2	1.69	400
ν (Poisson's ratio)	0.28	0.17
α (thermal expansion coefficient) 10^{-6} mt/mt^o C	2.5	0.5
ρ (density) g/cm^3	2.3	2.225

The dimensions and relevant parameters of the accelerometer are given in table 2.

Table 2: MEMS dimensions.

Parameter	Symbol	Value
Proof-mass size	CxCxt	463x463x2 μm^3
Length of beam	L	457µm
Length of beam	b	90µm
Beam Width	w_a	2µm
Beam Width	w_b	4µm
Gap of the capacitive system	h_0	2µm
Proof-mass thickness	t	2µm

III. THE GRAVITATIONAL SEARCH ALGORITHM

GSA is a novel heuristic [28] optimization method which has been proposed by E. Rashedi and all in 2009 [29]. The basic physical theory which GSA is inspired from is the Newton's theory that states: Every particle in the universe attracts every other particle with a force that is directly proportional to the product of their masses and inversely proportional to the square of the distance between them [30].

The algorithm considers agents as objects consisting of different masses proportional to their value of fitness function. During generations, all these objects attract each other by the gravity force, and this force causes a global movement of all objects towards the objects with heavier masses. Hence, masses cooperate using a direct form of communication, through gravitational force. The heavy masses - which correspond to good solutions - move more slowly than lighter ones, this guarantees the exploitation step of the algorithm; the GSA was mathematically modeled in [29-32].

GSA algorithm can be explained following steps

- Step 1: Initialisation

When it is assumed that there is a system with N (dimension of the search space) masses, position of the ith mass is described as follows. At first, the positions of masses are fixed randomly

$$X_i = \left(x_i^1, x_i^2, \ldots\ldots, x_i^n\right), \text{ i=}1,\ldots N \tag{8}$$

Where, xid is the position of the ith mass in dth dimension.

Step 2: Fitness Evaluation of All Agents

In this step, for all agents, best and worst fitness are computed at each epoch described as follows.

$$best(t) = \min_{j\in\{1,\ldots,N\}} fit_j(t)$$
$$worst(t) = \max_{j\in\{1,\ldots,N\}} fit_j(t) \tag{9}$$

Where fitj(t) is the fitness of the jth agent of t time, best(t) and worst(t) are best (minimum) and worst (maximum) fitness of all agents.

Step 3: Compute the Gravitational Constant (G(t))

In this step, the gravitational constant at t time (G(t)) is computed as follows.

$$G(t) = G_0 \exp\left(-a\frac{t}{T}\right) \tag{10}$$

Where G0 is the initial value of the gravitational constant chosen randomly, α is a constant, t is the current epoch and T is the total iteration number.

Step 4: Update the Gravitational and Inertial Masses

In this step, the gravitational and inertial masses are updated as follows.

$$mg_i(t) = \frac{fit_i(t) - worst(t)}{best(t) - worst(t)} \tag{11}$$

Where fiti(t) is the fitness of the ith agent of t time.

$$Mg_i(t) = \frac{mg_i(t)}{\sum_{j=1}^{N} mg_i(t)} \tag{12}$$

Where Mgi(t) is the mass of the ith agent of t time.

Step 5: Calculate the Total Force

In this step, the total force acting on the ith agent (Fid (t)) is calculated as follows.

$$F_i^d(t) = \sum_{j\in kbest\ j\neq i} rand_j F_{ij}^d(t) \tag{13}$$

Where randj is a random number between interval [0, 1] and kbest is the set of first K agents with the best fitness value and biggest mass.

The force acting on the ith mass (Mi(t)) from the jth mass (Mj(t)) at the specific t time is described according to the gravitational theory as follows.

$$F_{ij}^{d}(t) = G(t)\frac{M_i(t)M_i(t)}{R_{ij}(t)+\varepsilon}\left[x_j^d(t) - x_j^d(t)\right] \tag{14}$$

Where Rij(t) is the Euclidian distance between ith and jth agents $\left(\left\|x_i(t), x_j(t)\right\|_2\right)$ and ε is the small constant.

Step 6: Calculate the Acceleration and Velocity

In this step, the acceleration (aid (t)) and velocity (vid (t)) of the ith agent at t time in dth dimension are calculated through law of gravity and law of motion as follows.

$$a_i^d(t) = \frac{F_i^d(t)}{Mg_i^d(t)} \tag{15}$$

$$v_i^d(t+1) = rand_i.v_i^d(t) + a_i^d(t) \tag{16}$$

Where randi is the random number between interval [0,1].

Step 7: Update the Position of the Agents

In this steps the next position of the ith agents in dth

(xid(t+1)) dimension are updated as follows.

$$x_i^d(t+1) = x_i^d(t) + v_i^d(t+1) \tag{17}$$

The principal of the GSA is shown in Figure 11.

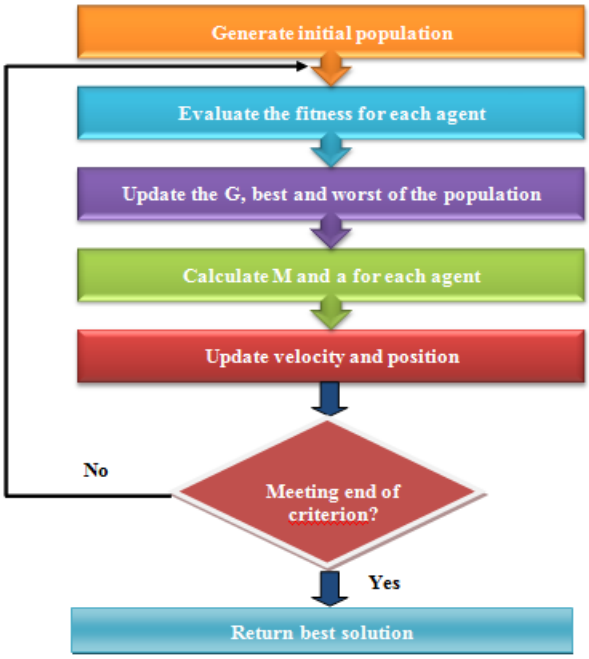

Figure 11. GSA Algorithm flowchart.

IV. FORMULATION OF THE OBJECTIVE FUNCTION OF ACCELEROMETER MODEL AND ITS VALIDATION

IV.1 Formulation of the objective function

The employment of the GSA algorithm follows a very simple iterative technique to minimize an objective function, given by ha. The details of this objective function will be explained later. The design variables are represented by ha.

ha = {V, K, a, A}

where

$$h_a = h_0\left(\frac{1-\frac{ma}{kh_0}}{3}\left(1+2\cos\left\{\frac{1}{3}\cos^{-1}\left[1-\frac{2}{(1-I)^3}\frac{\frac{1}{2}\frac{\varepsilon A}{k}V^2}{G_{pi}}\right]\right\}\right)\right) \quad (18)$$

To apply the GSA we, we take random values for the design variables within the following ranges. These ranges were chosen based on the minimum size constraints and maximum area

constraints, in addition to general observation and intuition about the final design's optimal geometry.

In the case the Proof-mass without holes

$$\begin{cases} A \epsilon \left(2.10^{-7}; 3.10^{-7}\right) \\ V \epsilon (1;2) \\ K \epsilon (1;6) \\ a \ \epsilon (800;4000) \end{cases}$$

In the case the Proof-mass with holes

$$\begin{cases} n \ \epsilon (1;25) \\ V \epsilon (1;2) \\ K \epsilon (1;6) \\ a \epsilon (800;4000) \end{cases}$$

where

A : Effective area of movable plate

V: voltage

K : spring of stiffness

a : applied acceleration

n: number of holes

IV.2. Results and discussion

In this section, the simulation was performed using the GSA, the value of gravitational search algorithm parameters is given in table 3. By applying the Gravitational search algorithm we have obtained the optimal values for A, K, a,V, n, ha. In this method we have used totally three thousand iterations to obtain the optimal design. The optimization process has maximized the (ha), represented by the objective or fitness function ha, by satisfying the design criteria. The best performing design was saved for each successive starting population to converge on the optimum values. The results had been displayed for the following iterations and the optimum values obtained by the GSA algorithm have also been described in the tables 4 and 5.

The iterative Gravitational search algorithm process minimizes the h_a, represented by the objective function ha, while satisfying all other design criteria. The best performing design is saved for each successive starting population to converge on the optimum values. Figures 12, 14,16,18, 20 and 22 illustrates this fact by displaying the optimum value of the objective function

for the first 300 starting populations. Clearly, the GSA algorithm succeeds in progressively finding designs with smaller design areas. Additionally, the GSA algorithm appears to converge to the best design. As shown in the figure (12-23).

After 300 starting populations of 300 generations have been computed, the five best performing designs are output to the user. The final results are shown in Tables 4 and 5. Note that A converges to 2.10-7 m, the minimum value possible. Although 20 μm is never achieved exactly (due to the exclusive nature of the random generator function) it can be assumed that the optimum design has V=2Volts. Conversely, K and a do not appear to converge to a value. This must imply that there is a range of optimum values that can be used to achieve the best design. As a result, the optimum dimensions presented here are only one set of the possible values.

We note from the results obtained using Gravitational search algorithm that the design parameters mainly affect the voltage value as show in the figure 12 to 17.

Figure 12 to 17 shows the response of the suspended mass and design parameters effects, figure 12 and 13 show a stable gap of 2.3389 μm, corresponding to the voltage applied. When the parallel - plate actuator is then exposed to an acceleration of 2069.6 m/s^2 in interval 800<a<3500, which corresponds to the pull - in acceleration at Vmax =1.9977 Volts and a spring of stiffness of 3.8064 N/m with effective area of movable plate A=3.977x10-7 m².

Figure 15 and 16 show a stable gap of 2.1044 μm, when the acceleration max is 2661.6 m/s^2 in interval 800<a<4000, at Vmax =1.9669 Volts and a spring of stiffness of 3.7995 N/m with effective area of movable plate A=2.9983x10-7 m².

Figure 16 and 17 gives us the best result which is the result found analytically, it shows a stable gap of 2.0097μm corresponding to the voltage of 1.9513 volts and acceleration of 2215.5 m/s², when a spring of stiffness is 4.0301 N/m with effective area of movable plate A=3.977.10-7 m²

The variation of effective area of movable plate (A) can cause the border effects. These border effects which are the electric field depending on the size of the electrodes, the greater these, the effects are less important and the distance between the electrodes decreases, the influence of edge effects decrease.

Figures 18 to 23 show the effect of number of holes on a stable gap (h_a), when the number of holes increase the value of a stable gap (h_a) decrease for example in figure 18 and 19, when n=3 h_a= 5.7868μm, in figure 20 and 21, n=6 and h_a= 5.5722μm, in figure 22 and 23, when n= 9, h_a=5.1695μm.

To analyze the effects of the number of the holes on the capacitance and pull-in voltage of a parallel plate MEMS Accelerometer, numerical analysis holes effects are given.

The perforated plate leads to a reduction in mass per unit length of the structure by >20% as compared to the solid structures. The holes also lead to a change in the area moment of inertia. Therefore, since the natural frequency ωn of the structure is a function of mass and the geometry (area moment of inertia and length), the presence of perforations directly leads to a change in the natural frequency.

We noticed that the capacitance caused by the number of holes will be decreased and its quotient in the total capacitance will be decreased. If the gap between the plates, ha, is given, the deviation of the capacitance and the pull-in voltage will be increased as the length and width of the hole increases.

This must be considered when researchers design tunable capacitors; otherwise the pull-in voltage in fact will exceed the designed pull-in voltage, which will result in the failure or breakage of the fabricated of a parallel plate MEMS Accelerometer.

Table 3: Parameters setting for GSA.

GSA parameters	**Value**
Dimension of problem	05
Number of agents	150
Max-iteration.	300
Velocity	clock
Acceleration.	gateway node flag
Mass. Ma=Mp=Mi=M	time master node flag
Position of agents.	for internal clock synchronization
Distance between agents in search space.	for external clock synchronization

Table 4: Parameters design effects.

Optimal design parameters with Variable design parameters				**Best value**	**Corresponding figures**
A_{max} (m^2)	V_{max} (Volts)	k_{max} (N/m)	a_{max} (m/s^2)	h_{amax} (µm)	
$2.10^{-7}<A<4.10^{-7}$	(1<V<2)	(1<K<4)	(800<a<3500)	2.3389	Figure 12 and 13
$3.977.10^{-7}$	1.9977	3.8064	2069.6		
$2.10^{-7}<A<3.10^{-7}$	(1<V<2)	(1<K<4)	(800<a<4000)	2.1044	Figure 14 and 15
$2.9983.10^{-7}$	1.9669	3.7995	2998.3		
$2.10^{-7}<A<2.4.10^{-7}$	(1<V<2)	(1<K<4.05)	(800<a<3500)	2.0097	Figure 16 and 17
$2.3558.10^{-7}$	1.9513	4.0301	2215.5		

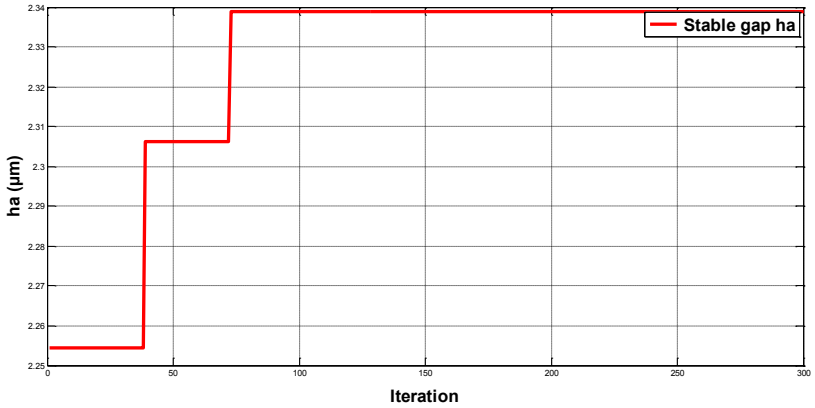

Figure 12. Interplate gap vs. iteration

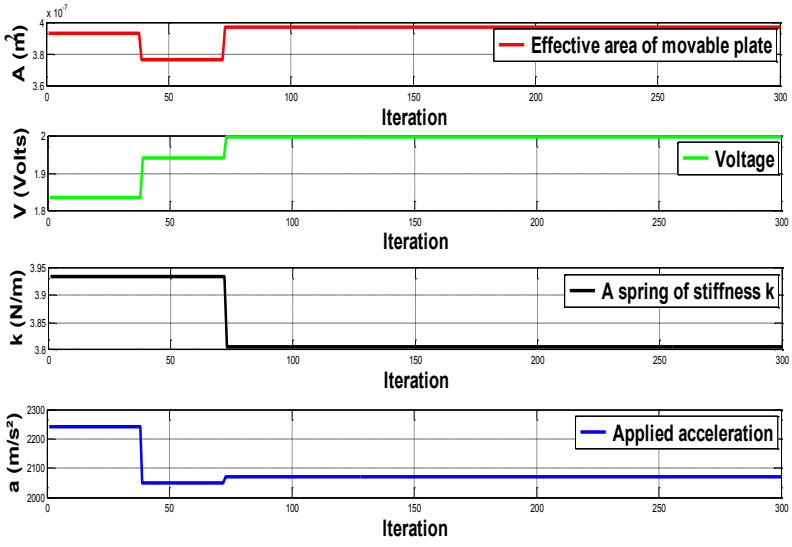

Figure 13. Design parameters vs. Iteration.

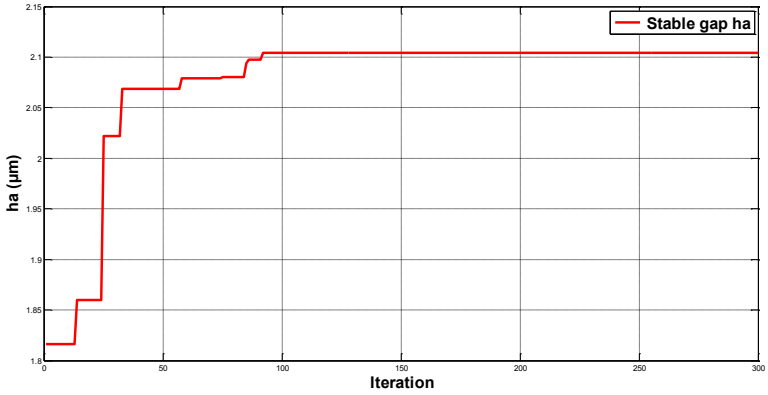

Figure 14. Interplate gap vs. iteration

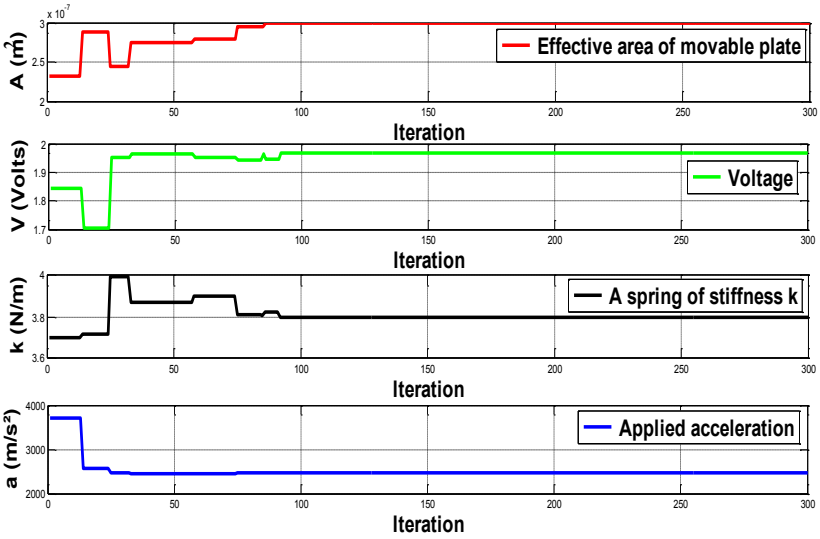

Figure 15. Design parameters vs. Iteration.

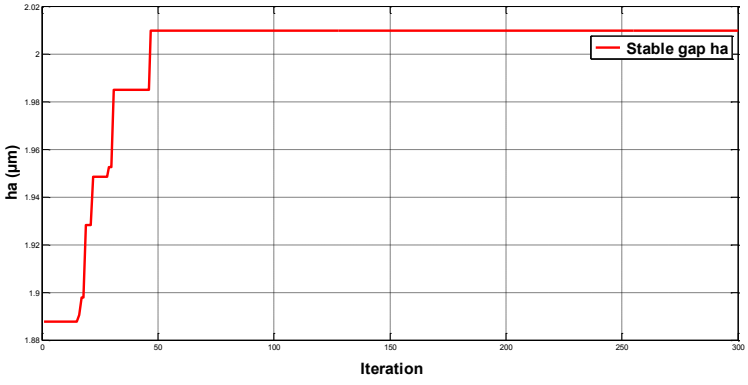

Figure 16. Interplate gap vs. iteration

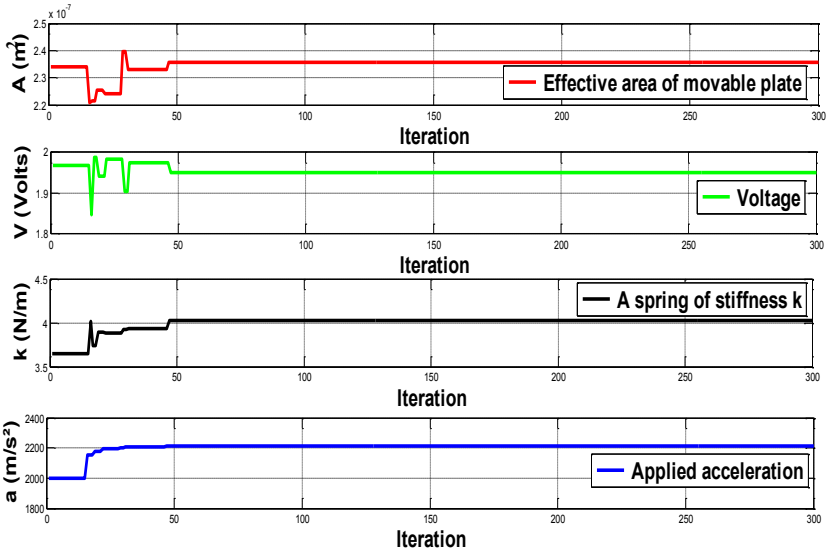

Figure 17. Design parameters vs. Iteration.

Table 5: The holes effects.

Optimal design parameters with Variable design parameters				**Best value**	**Corresponding figure**
n_{max}	V_{max} (Volts)	k_{max} (N/m)	a_{max} (m/s²)	$h_{a\ max}$ (µm)	
(1<n<5)	(1<V<2)	(1<K<4.05)	(800<a<3500)	5.7868	Figure 18 and 19
3	1.9979	3.9541	2036.9		
(1<n<10)	(1<V<2)	(1<K<4.05)	(800<a<3500)	5.5722	Figure 20 and 21
6	1.9981	3.9978	2204.7		
(1<n<20)	(1<V<2)	(1<K<4.05)	(800<a<3500)	5.1695	Figure 22 and 23
9	1.9905	3.9609	2174.3		

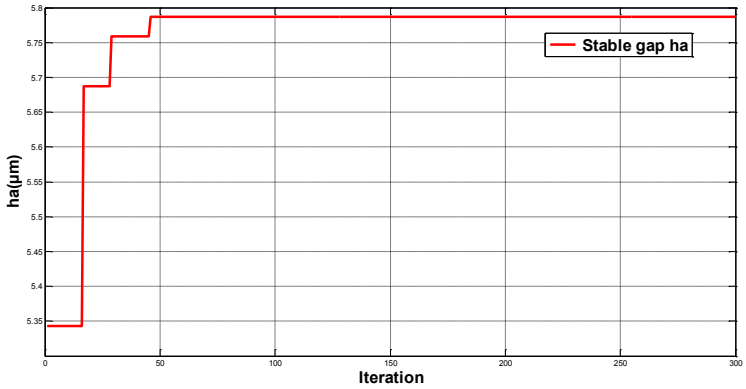

Figure 18. Interplate gap vs. iteration

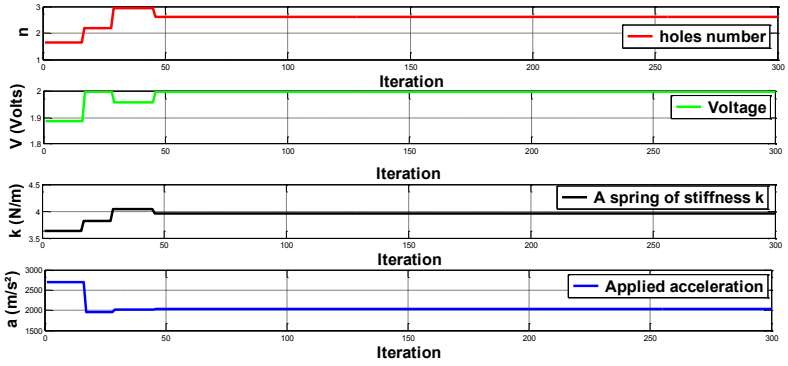

Figure 19. Design parameters vs. Iteration.

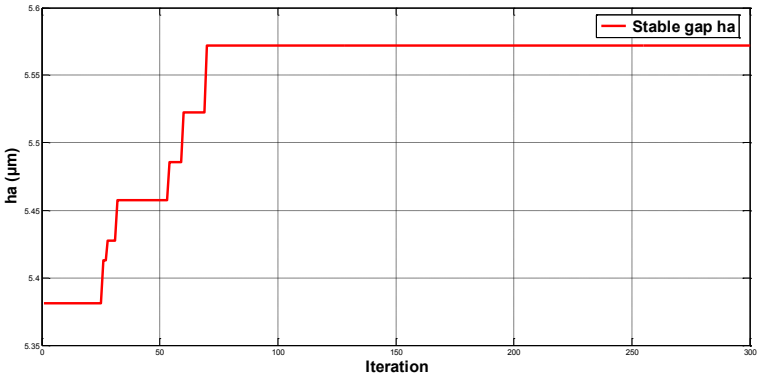

Figure 20. Interplate gap vs. iteration

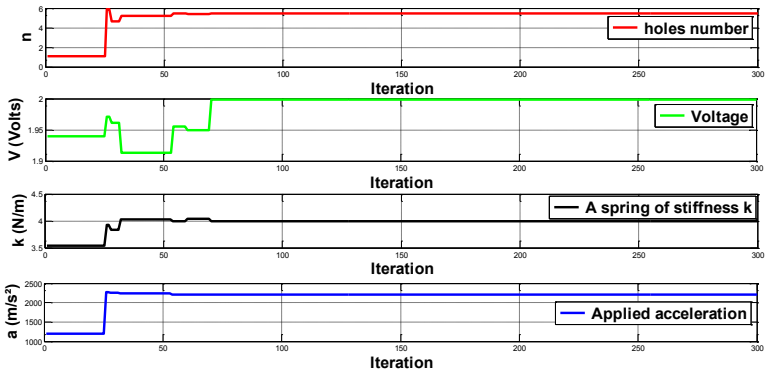

Figure 21. Design parameters vs. Iteration.

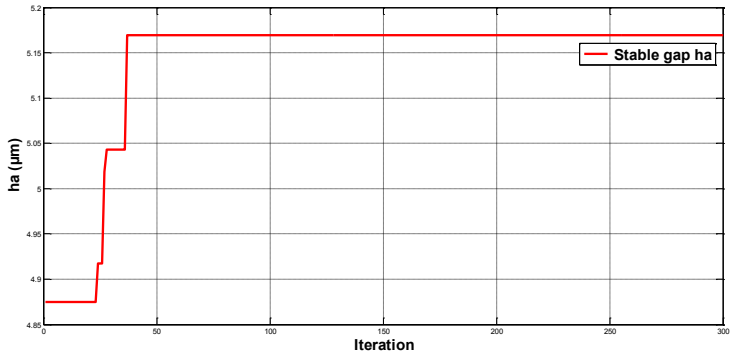

Figure 22. Interplate gap vs. iteration.

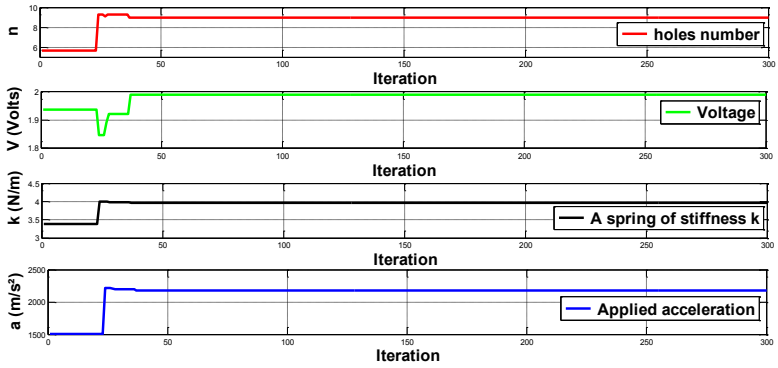

Figure 23. Design parameters vs. Iteration.

V. FINITE ELEMENT SIMULATIONS AND MODAL ANALYSIS OF L-SHAPED CANTILEVER PARALLEL - PLATE MEMS ACCELEROMETERS

A modal analysis was conducted to calculate the fundamental frequencies and modal shapes of the accelerometer. The boundary condition in the FEM simulation concerns the one edge of the short side which is constrained (displacement of x, y and z are zero, and rotation of x, y and z are zero) in the cantilevered L shaped MEMS. The finite element model (FEM) of a MEMS accelerometer is given by figure 24.

Figure 25 shows the frequencies modes of MEMS accelerometer obtained using Msc. Patran/Nastran software. The results gives the structure modal forms, and which makes it possible to see where are made the most deformations and which elements.

The colored fringes give the amplitude of the displacement vector describing the shape of each mode. The black color corresponds to null displacement and the red one presents the maximum amplitude.

Figure 25 shows the displacement of the MEMS accelerometer in Z direction, the maximum is about 2.003µm. The lowest frequency was in 1st mode (1061.6Hz), which gives the better the vibration direction. The frequency was increasing with each subsequent mode of vibration.

The translation in-plane modes, have a frequency around 6655.4Hz. The resulting modes from FEM simulations are the lowest frequency modes in the design and turns out to be at 1061.6Hz. The two following modes occur around 2111Hz and correspond to Out-of plane rotation. The rotation results in a tension (or compression) common to the four L-shaped beam. For small-displacements, the out-of-plane translation does not introduce any axial force in the L-shaped beam. The other modes are at frequencies high enough to guarantee low sensitivity.

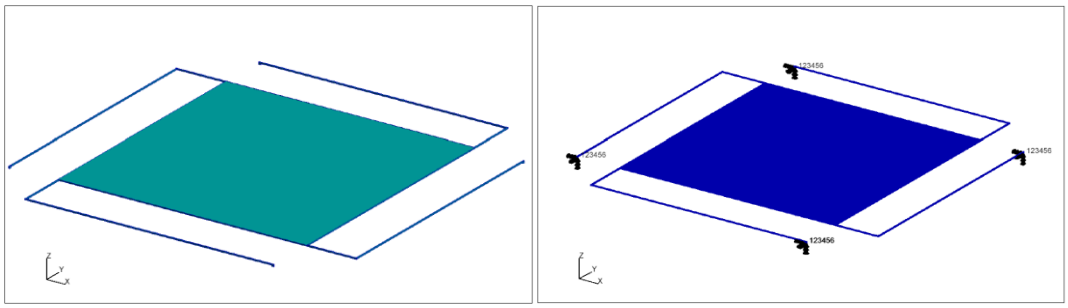

Figure 24. MEMS acceleromter FEM model.

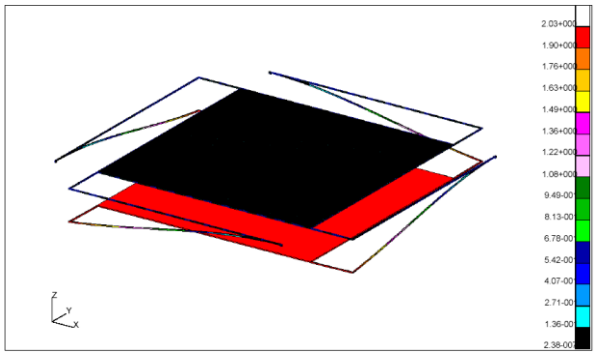

Mode 1, f1=1061.6Hz, Displacement field in Z direction.

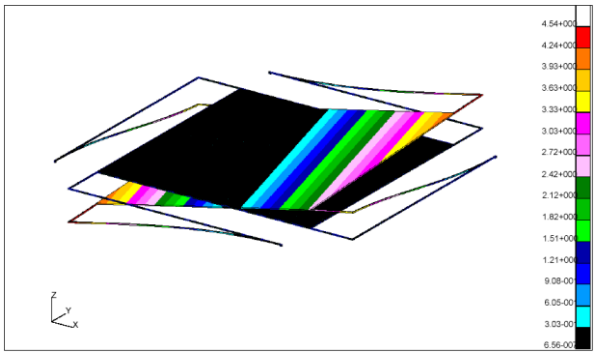

Mode 2, f2=2111Hz, Out-of plane rotation around the y-axis.

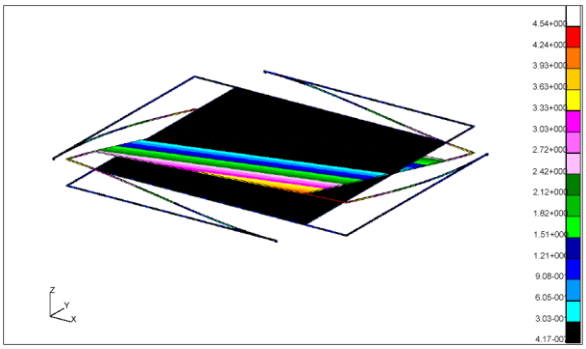

Mode 3, f3=2111Hz, Out-of plane rotation around the x-axis.

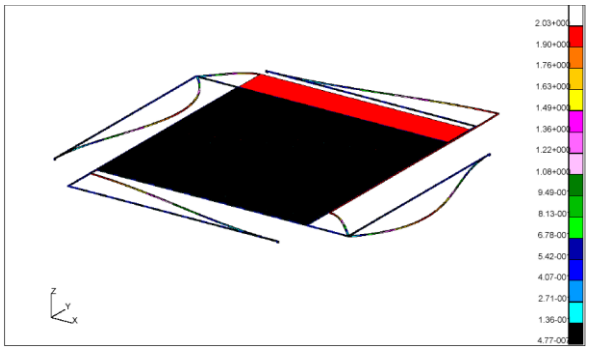

Mode 4, f4=6655.4Hz, In-plane translation in y- direction

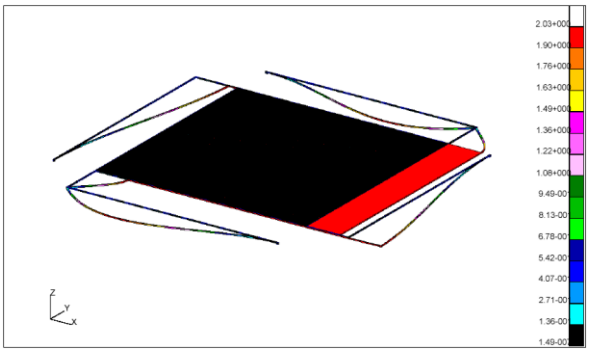

Mode 5, f5=6655.9Hz, In-plane translation in x-direction

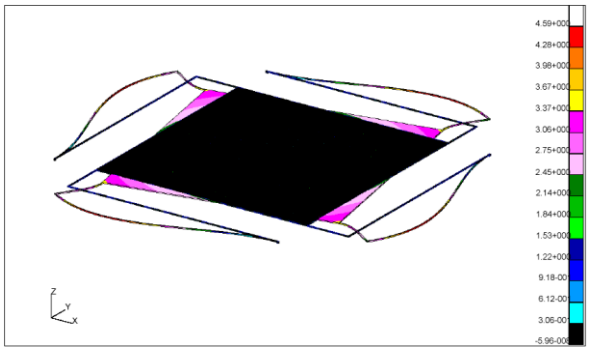

Mode 6, f6=15382Hz, In-plane rotation

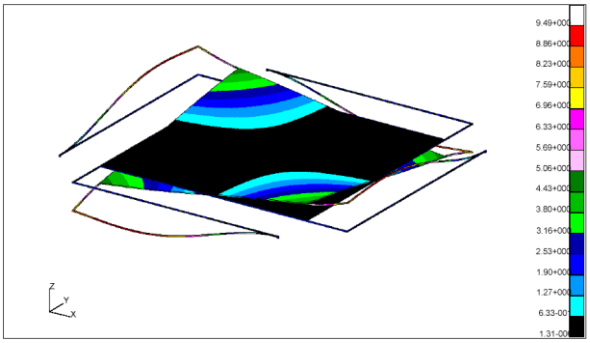

Mode 7, f7=39529Hz

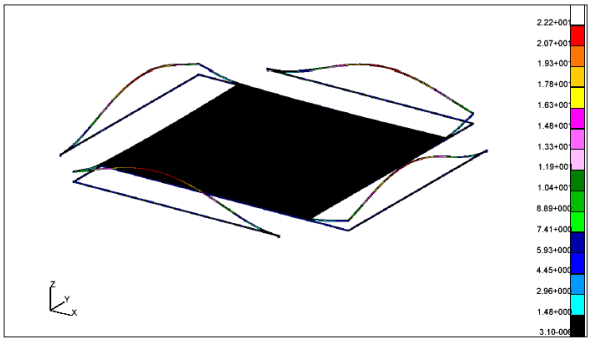

Mode 8, f8=49429Hz, mechanical mode of the spring.

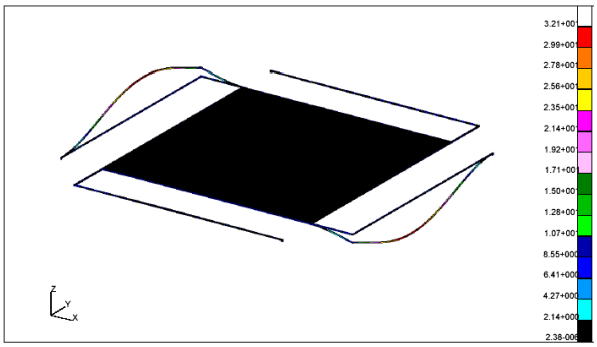

Mode 9, f9=50286Hz, mechanical mode of the spring.

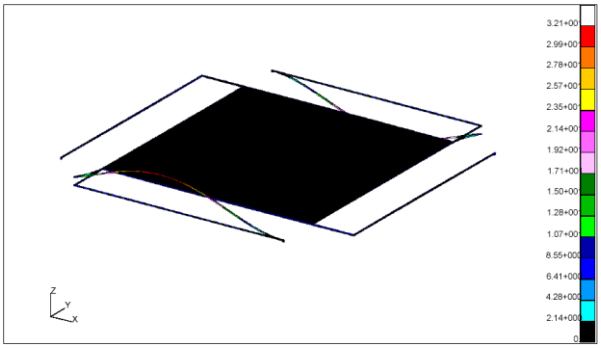

Mode 10, f10=50287Hz, mechanical mode of the spring

Figure 25. Various shape modes of the cantilevered L shaped MEMS.

VI. CONCLUSIONS

In this paper, we have proposed a system to perform the optimization of the design parameters in the L-shaped MEMS accelerometer. For this, we have employed a Gravitational Search optimization algorithm which provides an efficient optimization technique. The result shows that this method has delivered better results in terms of the fitness values. The simulation results also show that the intensity of the springs which is the weakest part in the accelerometer meets the

material intensity under the applied external accelerations in all directions. A modal analysis was used to extract the fundamental frequencies and modal shapes of the design as a reference for the range of operation of the device. The lowest natural frequency of the device is about 1061.6 Hz.

REFERENCES

[1] A. Zia, M.A.S Rahman, S.C. Mukhopadhyay, I. H. Al-Bahadly, P. L. Yu, C. Gooneratne, J. Kosel and T.S. Liao, MEMS Based Impedimetric Sensing of Phthalates, Proceedings of IEEE I2MTC 2013 conference, IEEE Catalog number CFP13IMT-CDR, ISBN 978-1-4673-4622-1, May 6-9, 2013, Minneapolis, USA, pp. 855-860.

[2] A. I. Zia, S. C. Mukhopadhyay, P.L. Yu, I.H. Al-Bahadly, C. P. Gooneratne, J. Kosel, "Post Annealing Performance Evaluation of Printable Interdigital Capacitive Sensors by Principal Component Analysis", IEEE Sensors Journal, 2014, http://dx.doi.org/10.1109/JSEN.2014.2355224.

[3] A. Sundaram, M. Maddela, R. Ramadoss, and L. Feldner, MEMS-Based electronically steerable antenna array fabricated using PCB technology, Microelectromechanical Systems, Journal of, vol. 17, no. 2, pp. 356-362, Apr. 2008.

[4] C-H. Han, D-H. Choi, and J-B. Yoon, Parallel-plate MEMS variable capacitor with superior linearity and large tuning ratio using a levering structure," Microelectromechanical Systems, Journal of, vol. 20, no. 6, pp. 1345-1354, Dec. 2011.

[5] M. Kraft, C. Lewis, T. Hesketh, and S. Szymkowiak, A novel micromachined accelerometer capacitive interface, Sensors and Actuators A: Physical, vol. 68, no. 13, pp. 466-473, Jun. 1998.

[6] Y. Fenglin, G. Shiqiao, Z. Jie, L. Haipeng, N. Shaohua, J. Lei , The vibration and measurement of driving mode of the two-stage decoupled micro-machined gyroscope, Int. J. Smart Sens. Intell. Syst. 6 (2013) 1599-1616.

[7] N. El-Bendary, Q. Tan, F. C. Pivot, A. Lam, Fall detection and prevention for the elderly: a review of trends and challenges, Int. J. Smart Sens. Intell. Syst. 6 (2013) 1230-1266.

[8] S. J. Kim, G. Flowers, C. Chen, and R. Dean, \Active vibration control and isolation for micro-machined devices," in ASME 2008 Conference on Smart Materials, Adaptive Structures and Intelligent Systems, Jan. 2008, pp. 657-664.

[9] Ding W., (2013), MEMS pressure sensor, Market & technology report, Yole Développement.

[10] Jeff Perkins, MEMS Everywhere: Sensing the world around you, and more Semicon West, Yole Developpement, 2012 available at http://www.semiconwest.org/sites/ semiconwest.org/files/docs/.

[11] L. M. Roylance and J. B. Angell, A Batch-Fabricated Silicon Accelerometer, IEEE Trans. Elec. Dev., ED-26, 1911 (1979).

[12] Trolier Mckinstry and P. Muralt, Thin film piezoelectrics for MEMS, J. Electroceramics, vol. 12, no. 1-2, pp. 7–17, 2004.

[13] T. Berther, G.H. Gautschi, J. Kubler, Capacitive accelerometers for static and low-frequency measurements, Sound and Vibration 30 (6)(1996) 28-30.

[14] H. Chen, S. Shen, M. Bao, Over-range capacity of a piezoresistive micro accelerometer, Sens. Actuators 58 (3) (1997) 197-201.

[15] G. H. Gautschi, Piezoelectric Sensorics. New York: Springer, 2002.

[16] Biter Boga, et al., Modeling of a capacitive Σ-Δ mems accelerometer system Including the noise components and Verification with test results, pp. 821 – 824, doi 10.1109/MEMSYS.2009.4805509-2009 ©IEEE.

[17] Yoshida, K.; Matsumoto, Y.; Ishida, M.; Okada, K. High-Sensitive Three Axis SOI Capacitive Accelerometer Using Dicing Method. Proceedings of Technical Digest of the 16th Sensor

Symposium, Toyohashi, Japan, 2–3 June 1998; pp. 25–28.
[18] Vincas Benevicius et al., Identification of Capacitive MEMS Accelerometer Structure Parameters for Human Body Dynamics Measurements, Sensors 2013, 13, 11184-11195; doi:10.3390/s130911184
[19] D.Ozevin et al., Resonant capacitive MEMS acoustic emission transducers, Smart Mater. Struct. 15 (2006) 1863–1871, doi:10.1088/0964-1726/15/6/041.
[20] H. Helvajian, ed, "Microengineering Aerospace Systems", The Aerospace Press, 1999
[21] S. Cass, "MEMS in Space", IEEE Spectrum, p.56, July 2001
[22] Robert Osiander, M. Ann Garrison Darrin, John L. Champion (Editors), "MEMS and Microstructures in Aerospace Applications", CRC (2005) 400 pages, Chapter 11, Micropropulsion technologies, J. Schein, pp. 229.
[23] Hoon Sohn et al., A Review of Structural Health Monitoring Literature: 1996–2001, Los Alamos National Laboratory Report, LA-13976-MS, 2004.
[24] T. Paul, J. Singh, M.M. Nayak, K. Rajanna, M.S. Kumar, Design and optimization of bulk micromachinaded accelerometer for space applications, Int. J. Smart Sens. Intell. Syst. 1 (2008) 1019-1030.
[25] J.S. Botero V, W. Hernández, E. Fernández, Orientation of a triaxial accelerometer using a homogeneous transformation matrix and kalman filters, Int. J. Smart Sens. Intell. Syst. 7 (2014) 1631-1646.
[26] R.R. Craig, A.J. Kurdila, Fundamentals of Structural Dynamics [M], Wiley.com, 2006.
[27] Ki Bang Lee, Principles of Microelectromechanical Systems, John Wiley & Sons, Inc., 2011.
[28] Esmat Rashedi, Hossein Nezamabadi, Saeid Saryazdi. GSA: A Gravitational Search Algorithm. Department of Electrical Engineering, Shahid Bahonar University of Kerman, P.O. Box 76169-133, Kerman, Iran. Information Sciences 179 (2009) 2232–2248.
[29] M. Ghalambaz, A.R. Noghrehabadi, M.A. Behrang, E. Assareh, A. Ghanbarzadeh, N.Hedayat, A Hybrid Neural Network and Gravitational Search Algorithm (HNNGSA) Method to Solve well known Wessinger's Equation, World Academy of Science, Engineering and Technology 73 2011.
[30] Serhat Duman, Yusuf Sonmez, Yusuf Sonmez, Application of Gravitational Search Algorithm for Optimal Reactive Power Dispatch Problem, pp. 519 – 523, 987-1-61284-922-5/11/$26.00©2011 IEEE.
[31] Mohammad Khajehzadeh and Mahdiyeh Eslami, Gravitational search algorithm for optimization of retaining structures, Indian Journal of Science and Technology, pp.1821-1827, Vol. 5 No. 1 (Jan 2012) ISSN: 0974- 6846.
[32] A.Chatterjee and G. K. Mahanti, Comparative performance of gravitational search algorithm and modified particle swarm optimization algorithm for synthesis of thinned scanned concentric ring array antenna, Progress in Electromagnetics Research B, Vol. 25, 331-348, 2010.